



### 저작자표시-비영리-동일조건변경허락 2.0 대한민국

이용자는 아래의 조건을 따르는 경우에 한하여 자유롭게

- 이 저작물을 복제, 배포, 전송, 전시, 공연 및 방송할 수 있습니다.
- 이차적 저작물을 작성할 수 있습니다.

다음과 같은 조건을 따라야 합니다:



저작자표시. 귀하는 원저작자를 표시하여야 합니다.



비영리. 귀하는 이 저작물을 영리 목적으로 이용할 수 없습니다.



동일조건변경허락. 귀하가 이 저작물을 개작, 변형 또는 가공했을 경우에는, 이 저작물과 동일한 이용허락조건하에서만 배포할 수 있습니다.

- 귀하는, 이 저작물의 재이용이나 배포의 경우, 이 저작물에 적용된 이용허락조건을 명확하게 나타내어야 합니다.
- 저작권자로부터 별도의 허가를 받으면 이러한 조건들은 적용되지 않습니다.

저작권법에 따른 이용자의 권리는 위의 내용에 의하여 영향을 받지 않습니다.

이것은 [이용허락규약\(Legal Code\)](#)을 이해하기 쉽게 요약한 것입니다.

[Disclaimer](#)

공학석사학위논문

**Density functional study on the  
thermal stability of  $\text{RMn}_2\text{O}_5$   
( $\text{R}=\text{Bi}, \text{Y}, \text{Gd}, \text{Pr}$  or  $\text{Sm}$ )**

2015 년 2 월

서울대학교 대학원

기계항공공학부

Li, Chenzhe

**Density functional study on the  
thermal stability of RMn<sub>2</sub>O<sub>5</sub>  
(R=Bi, Y, Gd, Pr or Sm)**

지도교수 조 맹 효

이 논문을 공학석사 학위논문으로 제출함

2014 년 10 월

서울대학교 대학원

기계항공공학부

Li, Chenzhe

Li, Chenzhe 의 공학석사 학위논문을 인준함

2014 년 12 월

위원장 김 윤 영(인)

부위원장 조 맹 효(인)

위 원 조 경 재(인)

Density functional study on the  
thermal stability of RMn2O5

Feb. 2015

Li,  
Chenzhe

## **Abstract**

# **Density functional study on the thermal stability of $\text{RMn}_2\text{O}_5$ ( $\text{R}=\text{Bi}, \text{Y}, \text{Gd}, \text{Pr}$ or $\text{Sm}$ )**

Li, Chenzhe

School of Mechanical and Aerospace Engineering

The Graduate School

Seoul National University

High throughput computational screening methods based on density functional theory has been an extraordinary success, but calculating the thermal stability of heavy and rare earth evolved transition metal oxide compounds still remain a challenge. In this work, by using a mixed GGA and GGA+U method, we have investigated the heavy and rare earth elements effect on predicting thermal stability of  $\text{RMn}_2\text{O}_5$  ( $\text{R}=\text{Bi}, \text{Y}, \text{Gd}, \text{Pr}$  or  $\text{Sm}$ ) compounds.

The temperature phase diagram constructed from the DFT simulation without R site correction are demonstrate to show good prediction on the decomposition

reactions, but the predicted temperature gives an underestimation comparing to the existing experimental data. The *d/f* orbital charge of R site elements indicate uncorrected rare earth elements could induce certain amount of simulation inaccuracy similar to transition metal elements and the amount of charges in these orbitals shows liner relationship with the prediction error. Our GGA+U correction results demonstrate that further correction on R site elements (same to transition metal elements) could effectively improve the accuracy of thermal stability prediction without introducing other high computational cost methods.

**Keywords:** DFT, Thermal stability prediction, Rare earth elements

**Student Number:** 2013-22496

# Contents

<b>Abstract</b>	i
Nomenclatures	iv
List of Figures	v
List of Tables	vii
<b>Chapter 1 Introduction</b>	1
<b>Chapter 2 Methodology</b>	3
<b>2.1 Computational Methods</b>	3
<b>2.2 Energy Corrections</b>	5
<b>2.3 Structure thermal stability calculation</b>	8
<b>Chapter 3 Result and Discussion</b>	10
<b>3.1 Lattice parameters</b>	10
<b>3.2 Thermal stability</b>	12
<b>3.2.1 BiMn<sub>2</sub>O<sub>5</sub></b>	12
<b>3.2.2 RMn<sub>2</sub>O<sub>5</sub> (R=Pr, Sm, Gd or Y)</b>	15
<b>3.3 Error Analysis</b>	18
<b>Chapter 4 Conclusion</b>	23
Bibliography	24
초 록	29

## Nomenclatures

$U$	Coulomb and exchange parameters
$\Delta E_j$	Energy adjustment value for element $j$
$c_j$	Element fraction for $j$ in the compounds
$E^{\text{GGA+U}}$	Total energy of oxide compounds calculated from the GGA+U simulation
$E_i^{\text{GGA}}$	Pure element energy per atom calculated by GGA method
$n_i$	Number of $i$ atoms in the oxide compound
$\Delta E^{\text{GGA+U}}$	Formation energy before energy correction
$\Delta H^{\text{Expr.}}$	Binary oxides experimental value
$\Delta H_{\text{RMO}}$	Formation enthalpy of the ternary compounds
$\zeta$	Transition metal elements that applied the energy correction
$\mu_i$	Chemical potential of element $i$
$\mu_{\text{RMO}}^0$	Chemical potential of ternary oxide compounds
$\Delta\mu_i$	Change of chemical potential for element $i$

## List of Figures

**Figure 1** a) Crystal structure indication of  $\text{RM}_2\text{O}_5$ - $\delta$  compounds ( $\delta = 0$ ). Atoms are labelled with their Wyckoff symbols. b) edge-shared  $\text{MO}_5$  distorted tetragonal pyramid in  $\delta = 0$  type of structures and c) vertex-sharing  $\text{MO}_4$  tetrahedral in  $\delta = 0.5$  type of structures.

**Figure 2** Spinning configurations of  $\text{Mn}^{3+}$  as well as  $\text{Mn}^{4+}$  in the  $\text{RMn}_2\text{O}_5$  compounds.

**Figure 3** Difference between experimental and calculated manganese binary oxides formation enthalpies ( $\Delta H^{\text{Diff}}$ ) as a function of manganese content ( $c_{\text{Mn}}$ ). The dashed line is linearly fitted to the binary oxides data points; the slope of the fitted line represents the energy adjustment value  $\Delta E_{\text{Mn}}$ .

**Figure 4** Lattice constants of  $\text{RMn}_2\text{O}_5$ : a (black), b (red), c (blue) vs ionic radii of  $\text{R}^{3+}$  cation.

**Figure 5** Temperature phase diagram of  $\text{BiMn}_2\text{O}_5$  compounds.  $\Delta\mu_{\text{Mn}}$  is plotted as a function of temperature. Compounds considered in the figure are labeled to ① $\text{Bi}_2\text{O}_3$  ② $\text{MnO}_2$  ③ $\text{Mn}_2\text{O}_3$  ④ $\text{Mn}_3\text{O}_4$  ⑤ $\text{MnO}$  ⑥ $\text{BiMn}_7\text{O}_{12}$  ⑦ $\text{BiMnO}_3$ . (a) Overall temperature region and (b) zoomed high temperature fragment corresponding to the decomposition temperature.

**Figure 6** (a) TGA (Weight %, black) and DSC (Heat flow (W/g), red) curves of  $\text{BiMn}_2\text{O}_5$  dried powder. (b) TGA (Weight %, black) and DSC (Heat flow (W/g), red) curves of pure phase  $\text{BiMn}_2\text{O}_5$  near decomposition temperature range.

**Figure 7** Temperature phase diagram of (a)PrMn<sub>2</sub>O<sub>5</sub>, (b) SmMn<sub>2</sub>O<sub>5</sub>, (c)GdMn<sub>2</sub>O<sub>5</sub> and (d)YMn<sub>2</sub>O<sub>5</sub> compounds.  $\Delta\mu_{Mn}$  is plotted as a function of temperature. Compounds considered in the figure are labeled to ①R<sub>2</sub>O<sub>3</sub> ②MnO<sub>2</sub> ③Mn<sub>2</sub>O<sub>3</sub> ④Mn<sub>3</sub>O<sub>4</sub> ⑤MnO ⑥PrMn<sub>7</sub>O<sub>12</sub> ⑦RMnO<sub>3</sub> ⑧Y<sub>2</sub>Mn<sub>20</sub>O<sub>7</sub> (R is corresponding to the simulated rare earth elements in the compounds).

**Figure 8** (a) Diagram of the calculated (red circle), experimental decomposition temperature (black square) of RMn<sub>2</sub>O<sub>5</sub> compounds as a function of R<sup>3+</sup> ionic Radii. (b) Difference between DFT prediction and experiment value of decomposition temperature (prediction error) as a function of R<sup>3+</sup> ionic Radii

**Figure 9** DFT predicted decomposition temperature as a function of onsite coulomb correction value U: (a) PrMn<sub>2</sub>O<sub>5</sub>, (b) SmMn<sub>2</sub>O<sub>5</sub>, (c)GdMn<sub>2</sub>O<sub>5</sub> and (d)YMn<sub>2</sub>O<sub>5</sub> compounds.

## List of Tables

**Table 1** Crystal Structures, magnetic configurations, experimental and simulated formation enthalpy of the binary oxide compounds

**Table 2** GGA+U calculated energy difference between different spinning configurations (per formula unit). FM spinning configuration is set as the standard value

**Table 3** Experimental and theoretical lattice constants of  $\text{RMn}_2\text{O}_5$  (R=Y, Pr, Sm, Gd, Bi)

**Table 4** Temperature difference between experiment and simulation and orbital charge for  $\text{R}^{3+}$  ions in  $\text{RMn}_2\text{O}_5$

**Table 5** Simulated and experiment decomposition temperature after R site ion U correction

## Chapter 1 Introduction

Within the last few decades, new types of oxide materials were developed to reduce the usage of precious metal in the application of catalysts, sensors as well as batteries.<sup>1-3</sup> Despite of the great achievements in scientific research, long-term stability and their thermal endurance in the application ambient are rarely reported in published journals.<sup>2</sup> Contrast to performing long time-scale, high costs stability research, first principle simulations can provided a cost friendly way to the thermal properties investigation of the targeting materials. Previous articles have shown certain accuracy on predicting the thermal stability of battery cathode oxide materials, transition metal oxidation energy and formation enthalpies of numerous transition metal oxides.<sup>4-6</sup> However, the studies are limited in the alkaline transition metal oxide materials and few studies had considered the thermal stability prediction of materials involved rare-earth (RE) and heavy metal elements.<sup>7, 8</sup> This situation may partially owing to the ambiguous error introduced by the localized  $4f/d$  electrons in heavy elements, lack of as well as expensive simulation methods for getting the accurate formation enthalpies such as hybrid-functional methods or GW methods.<sup>9, 10</sup> Moreover, different from the alkaline oxides as well as light transition metal oxides, most of the working environment of materials include RE and heavy elements range from inter-medium temperature to high temperature (400~1000 °C) such as  $\text{LaMnO}_3$  for solid oxide fuel cells or  $\text{SmMn}_2\text{O}_5$  as De- $\text{NO}_x$  catalysts for diesel engines where proper experiments on investigating the thermal stabilities could hardly be carried out for large scale

material screening.<sup>3, 11</sup> Therefore, a high efficiency though-output methodology is needed for predicting the accurate heavy element thermal stabilities.

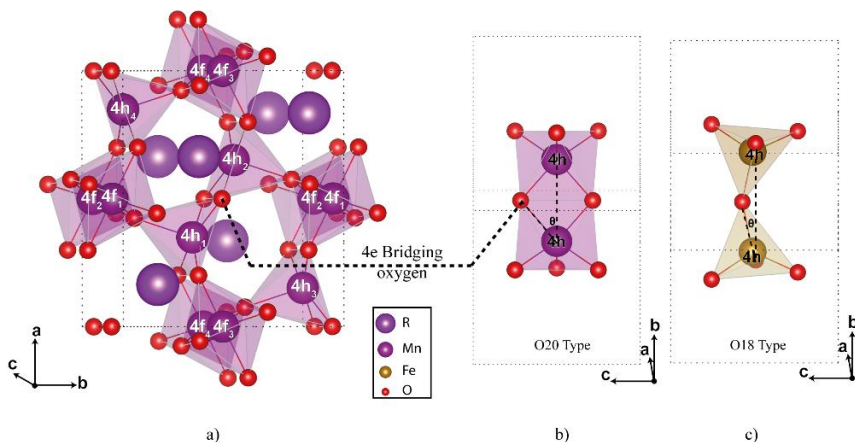


**Figure 1** a) Crystal structure indication of  $RM_2O_{5-\delta}$  compounds ( $\delta = 0$ ). Atoms are labelled with their Wyckoff symbols. b) edge-shared  $MO_5$  distorted tetragonal pyramid in  $\delta = 0$  type of structures and c) vertex-sharing  $MO_4$  tetrahedral in  $\delta = 0.5$  type of structures.

Recently, oxide compounds like  $RM_2O_{5-\delta}$  ( $R = Bi, Y$  or rare-earth elements;  $M = Mn, Fe, Al$  or  $Ga$ ) of mullite type structure (Shown in Figure 1) have come to spotlight in recent years due to the discovery of their multiferroicity, catalytic activity and many other properties.<sup>3, 12-14</sup> Among the mullite type structures,  $RMn_2O_5$  compounds are particularly ideal for first principle thermal dynamic investigations. As shown in Fig. 1, structures of  $RMn_2O_5$  compounds belong to one of the orthorhombic structures with the  $Pbam$  space group. Edge-sharing  $MnO_6$  octahedra Mullite chain aligned along the c-axis and inter-connected by the edge-sharing  $MnO_5$  distorted tetragonal pyramid polyhedron in the ab-plane. The void between the Mn polyhedron networks are therefore filled with the R

site elements. The R-site of  $\text{RMn}_2\text{O}_5$  compounds can be almost all the rare earth and heavy elements while the crystalline phase is preserved.<sup>15</sup> Thus, varying the R-site in the structure enables us to study the error effect on the thermal properties brought up by the rare earth and heavy elements.

## Chapter 2 Methodology

### 2.1 Computational Methods

First principle simulations in this article are carried out through employing the density functional theory with spin-polarized generalized gradient approximation (GGA) embedded in Vienna ab-initio simulation package (VASP).<sup>16,17</sup> Plane-wave basis and projector augmented-wave pseudopotentials (PAW) are used in the calculation.<sup>18</sup> The valence electron configurations in the pseudopotentials are considered in the following manners; Bi:  $5d^{10}6s^26p^3$ , Sm/Pr:  $5s^25p^65d^16s^2$ , Gd:  $5p^65d^16s^2$ , Y:  $4s^24p^64d^24f^05s^1$ ; Mn:  $3d^54s^2$ , and O:  $2s^24p^4$ . To correct the self-interaction errors of the strongly correlated electron systems, GGA+U method are also employed in our calculations.<sup>19</sup> The effective on site Coulomb and exchange parameters are set to 3.9 eV for Manganese since previous work indicating such parameter provides accurate oxidation energy in the oxide systems.<sup>5</sup> All the structures in our calculations are relaxed till reaching a force criteria of 0.005 eV/Å. High energy cut-off of 550 eV and a fine auto-generated  $\Gamma$ -centered k-space sampling mesh with a density of  $0.02\text{\AA}^{-1}$  for each direction are used to assure an accurate total energy for all the simulated system.<sup>20</sup>

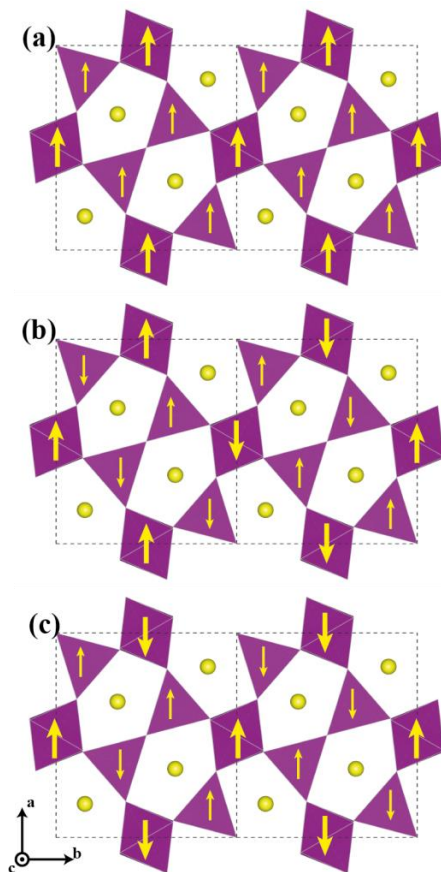


**Figure 2** Spinning configurations of  $\text{Mn}^{3+}$  as well as  $\text{Mn}^{4+}$  in the  $\text{RMn}_2\text{O}_5$  compounds. Furthermore, in this study, the magnetic structures of the oxide compounds are also taken into account to further promote the accuracy (see Table 1). For  $\text{RMn}_2\text{O}_5$  compounds, three different spinning configurations (shown in Figure 2) have been considered in our simulation according to the previous studies.<sup>21-</sup>

23

**Table 1** Crystal Structures, magnetic configurations, experimental and simulated formation enthalpy of the binary oxide compounds

(A)BO	Space Group	Magnetic Structure	$\Delta H^{\text{Expr.}}$ (eV)	$\Delta H_{\text{RMO}}$ (eV)
-------	-------------	--------------------	--------------------------------	------------------------------

MnO	Fm-3m	AFM <sup>24</sup>	-4.008	-4.030
MnO <sub>2</sub>	P42/mnm	AFM <sup>25</sup>	-5.425	-5.273
Mn <sub>2</sub> O <sub>3</sub>	Pbca	AFM <sup>26</sup>	-9.979	-10.07
Mn <sub>3</sub> O <sub>4</sub>	I41/amd	FM <sup>27</sup>	-14.45	-14.516
Bi <sub>2</sub> O <sub>3</sub>	P121/C1	-	-5.943	-8.37
Y <sub>2</sub> O <sub>3</sub>	IA3-	-	-19.843	-20.146
Sm <sub>2</sub> O <sub>3</sub>	C12/M1	-	-18.984	-19.195
Pr <sub>2</sub> O <sub>3</sub>	P-3m1	-	-18.848	-18.601
Gd <sub>2</sub> O <sub>3</sub>	I213	-	-19.026	-19.874

Table 2 summarizes the energy differences between different spinning configurations. The simulated results agree with previous magnetic studies in RMn<sub>2</sub>O<sub>5</sub> compounds<sup>21-23</sup>. Therefore, spinning structures with the lowest energies are used throughout our simulation.

**Table 2** GGA+U calculated energy difference between different spinning configurations (per formula unit). FM spinning configuration is set as the standard value.

Compound Name	FM	AFM1 (meV)	AFM2 (meV)
YMn <sub>2</sub> O <sub>5</sub>	0	-135.799	-101.576
BiMn <sub>2</sub> O <sub>5</sub>	0	-172.124	-190.117
PrMn <sub>2</sub> O <sub>5</sub>	0	-202.058	-222.399
SmMn <sub>2</sub> O <sub>5</sub>	0	-231.667	-251.307
GdMn <sub>2</sub> O <sub>5</sub>	0	-117.002	13.3105

## 2.2 Energy Corrections

The Coulomb exchange parameters are usually not universal between different valences of transition metal-ions. Therefore, further energy correction is usually used to achieve the experimental comparable data for further analysis. The energy correction we adopt in this article is similar to the previous reports on GGA/GGA+U hybrid energy correction.<sup>4</sup> Due to the inconstancy of the simulation package, the correction parameters are recalculated and introduced as follows:

We first adopt the 1.36 eV energy corrections on the oxygen total energy to cancel the over-binding problem as previously mentioned.<sup>5</sup> Then, energy adjustment ( $\Delta E_j$ ) value of elements that applied U corrections are obtained is obtained by linear fitting formation enthalpies difference between the binary oxides and simulated formation energy:  $\Delta H^{\text{Diff}}$  and the manganese fraction in the compounds:  $c_{Mn}$ . Eq. (1)~(2) is used for obtaining  $\Delta H^{\text{Diff}}$ ,

$$\Delta E^{\text{GGA+U}} = E^{\text{GGA+U}} - \sum_{i \in \zeta} n_i E_i^{\text{GGA}} \quad (1)$$

$$\Delta H^{\text{Diff}} = \Delta H^{\text{Expr.}} - \Delta E^{\text{GGA+U}} \quad (2)$$

where  $\Delta E^{\text{GGA+U}}$  is the calculated formation energy before energy correction;  $E^{\text{GGA+U}}$  is the total energy of oxide compounds calculated from the GGA+U simulation;  $\zeta$  is the oxide compounds atom species;  $n_i$  is the number of  $i$  atoms and  $E_i^{\text{GGA}}$  is the pure element energy per atom calculated by GGA method: that is the metallic form of Mn or oxygen molecular. In Eq. (2),  $\Delta H^{\text{Expr.}}$  is the known as the binary oxides experimental value in the existing publications.<sup>28</sup>

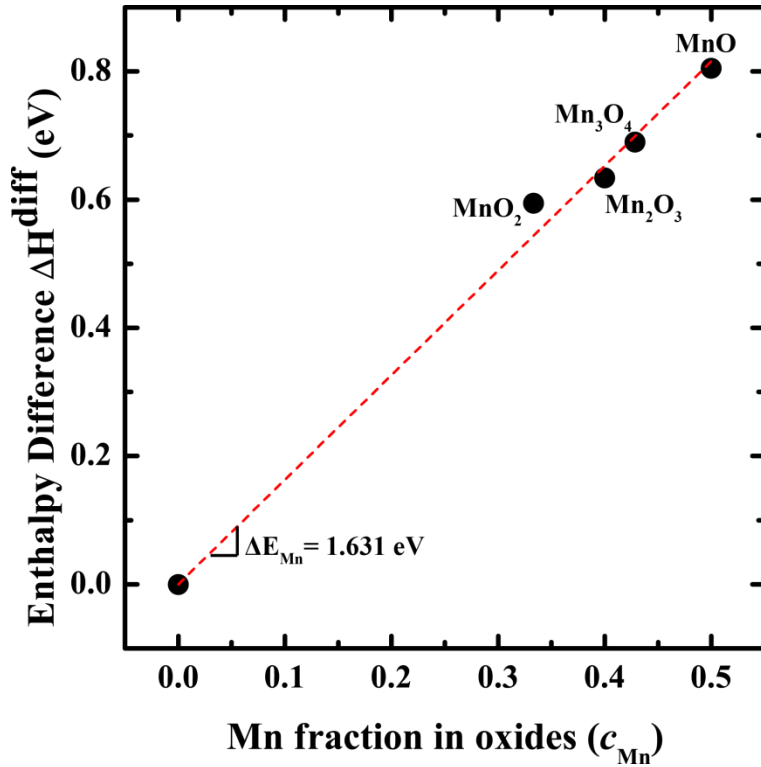


**Figure 3** Difference between experimental and calculated manganese binary oxides formation enthalpies ( $\Delta H^{Diff}$ ) as a function of manganese content ( $c_{Mn}$ ). The dashed line is linearly fitted to the binary oxides data points; the slope of the fitted line represents the energy adjustment value  $\Delta E_{Mn}$ .

The obtained energy adjustment value  $\Delta E_{Mn}$  is calculated to be 1.631 eV (shown in Figure 3), which is slightly smaller than the previously reported value 1.678 eV.<sup>4</sup> We consider such minor difference comes from the inconsistency of simulation package as well as the pseudopotentials.

Formation enthalpy of the oxide compounds therefore could be obtained in the following manner

$$\Delta H_{RMO} = E_{RMO}^{GGA+U} - \left( \sum_{i \in \zeta} n_i E_i^{GGA} + \sum_{j=\varsigma} n_j \Delta E_j \right) \quad (3)$$

Here,  $\Delta H_{RMO}$  denote to the formation enthalpy of the ternary compounds and  $\zeta$  is the transition metal elements that applied the energy correction, e.g. manganese. Formation enthalpies for the binary compounds after correction are also listed in Table 1 for reference.

### 2.3 Structure thermal stability calculation

To calculate the thermal stability of the ternary compounds, we start with assuming the chemical potential of the compounds remains constant in the compounds. Therefore, Eq. (4) should be fulfilled.

$$\sum_{i \in \zeta} \mu_i = \mu_{RMO}^0 \approx E_{RMO}^{GGA+U} \quad (4)$$

We are aware of the fact that chemical potential  $\mu_{RMO}^0$  is a function of temperature, and affected by the entropy effects. Calculation of such properties is usually time-consuming and contrary to our aim of developing high efficient thought-output simulation methods. Therefore, for solid phase compounds, we have simplified the potential  $\mu_{RMO}^0$  into the free energy calculated by first principle simulations:  $E_{RMO}^{GGA+U}$ . Such simplification have been proven to be effective since vibrational and entropy contribution are usually found to have minor effect on the system total energy.<sup>6, 7, 29</sup>

As shown in Eq. (4), direct relationship between the system chemical potential and the calculated system total energy from the first principle simulation are

obtained. We therefore could set the chemical potential  $\mu_i$  by referring to the pure element energy:  $E_i^{GGA}$ , resulting relationship:

$$\mu_R = \Delta\mu_R + E_R^{GGA} \quad (5)$$

$$\mu_{Mn} = \Delta\mu_{Mn} + \Delta E_{Mn} + E_{Mn}^{GGA} \quad (6)$$

$$\mu_O = \Delta\mu_O + \frac{1}{2}E_{O_2}^{GGA} \quad (7)$$

In Eq. (7), we use the above-described energy correction to the transition metal element: Mn to link between GGA and GGA+U method calculated energy. On the left hand side of Eq. (5), since gaseous phase entropy contribution is not negligible, Eq. (9) is used to consider the temperature and partial pressure effect on the oxygen chemical potential.

$$\Delta\mu_O = \frac{1}{2} \left[ \Delta H_{O_2}^{gas}(T, p^0) + kT \ln\left(\frac{p}{p^0}\right) - T^0 \Delta S_{O_2}^{gas}(T^0, p^0) \right] \quad (8)$$

The enthalpy  $\Delta H_{O_2}^{gas}(T, p^0)$  as well as entropy  $\Delta S_{O_2}^{gas}(T^0, p^0)$  difference of oxygen gas phase are taken from the experimental value of NIST-JANAF thermochemical tables.<sup>30</sup> Such treatment enables us to take the temperature as well as oxygen partial pressure into consideration.

To evaluate the stability of the  $RMn_2O_5$  compounds, the stable region in the chemical potential phase diagram is confined by using the following equations to ensure that no other phases are energetically favorable.

$$\mu_i \leq E_i^{GGA} \quad (9)$$

$$x \cdot \mu_{Mn} + y \cdot \mu_O \leq E_{Mn_xO_y}^{GGA+U} \quad (10)$$

$$x \cdot \mu_R + y \cdot \mu_O \leq E_{R_xO_y}^{GGA+U} \quad (11)$$

$$a \cdot \mu_R + b \cdot \mu_{Mn} + c \cdot \mu_O \leq E_{R_aMn_bO_c}^{GGA+U} \quad (12)$$

Eq. (10) gives the expression that no precipitates or evolution of pure element happens in the pure phase metal oxides. Eq. (11)-(13) indicates that other tested oxide compounds are not energetically favorable under the chemical potential condition. Therefore, the regions that fulfill the boundary condition could be considered as the stable region of the tested compound and thermal stability of the tested compounds could be determined by taking temperature effect into consideration.

## Chapter 3 Result and Discussion

### 3.1 Lattice parameters

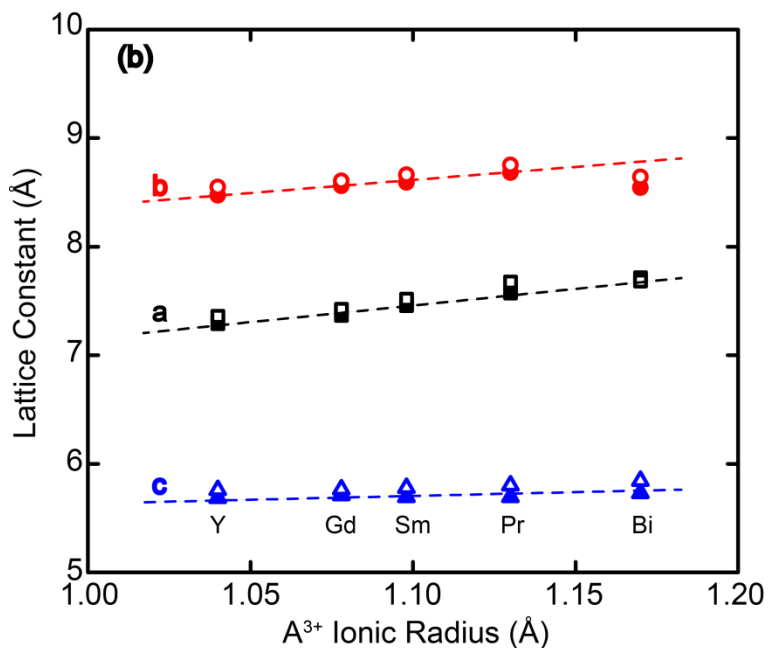


**Figure 4** Lattice constants of  $\text{RMn}_2\text{O}_5$ : a (black), b (red), c (blue) vs ionic radii of  $\text{R}^{3+}$  cation.

Simulated lattice constants are compared with the experimental results to confirm the simulation accuracy in Figure 4.<sup>21, 31-33</sup> Our simulations give good description to the crystal geometry comparing to our experimental observation. Slightly overestimation of the lattice parameter in the simulation is consistent to the previous GGA+U simulations since the parameter of the correction to the correlated d electrons is adjusted to the oxidation energy instead of the atomic geometry properties of manganese oxides.<sup>34</sup> Detailed simulated and experimental lattice parameters are presented in the Table 3

**Table 3** Experimental and theoretical lattice constants of  $\text{RMn}_2\text{O}_5$  (R=Y, Pr, Sm, Gd, Bi)

Sample	Experimental			Theoretical		
	a (Å)	b (Å)	c (Å)	a (Å)	b (Å)	c (Å)
$\text{YMn}_2\text{O}_5$	7.291	8.473	5.686	7.360	8.550	5.760
$\text{PrMn}_2\text{O}_5$	7.573	8.683	5.694	7.675	8.752	5.801
$\text{SmMn}_2\text{O}_5$	7.459	8.591	5.695	7.516	8.662	5.779
$\text{GdMn}_2\text{O}_5$	7.368	8.560	5.712	7.424	8.607	5.764
$\text{BiMn}_2\text{O}_5$	7.714	8.545	5.731	7.683	8.642	5.844

## 3.2 Thermal stability

### 3.2.1 $\text{BiMn}_2\text{O}_5$

$\text{BiMn}_2\text{O}_5$  is first considered among  $\text{RMn}_2\text{O}_5$  compounds in thermal stability simulations. Apart from the conventional binary compounds shown in Table S1, our simulations have also considered two more ternary compounds in Bi-Mn-O phase diagram:  $\text{BiMnO}_3$  and  $\text{BiMn}_7\text{O}_{12}$ . According to the constrain in Eq. (5), only two variables are independent to each other:  $\Delta\mu_{Mn}$  and  $\Delta\mu_O$ . Utilized the methodology introduced in the previous sections, boundary conditions for stable  $\text{BiMn}_2\text{O}_5$  (No other phases are stable.) are further derived as follows:

$$2\Delta\mu_{Mn} + 5\Delta\mu_O \geq \Delta H_{\text{BiMn}_2\text{O}_5} \quad (15)$$

$$\Delta\mu_O \leq 0 \quad (16)$$

$$\Delta\mu_{Mn} + \Delta E_{Mn} \leq 0 \quad (17)$$

$$x\Delta\mu_{Mn} + y\Delta\mu_O \leq \Delta H_{\text{Mn}_x\text{O}_y} \quad (18)$$

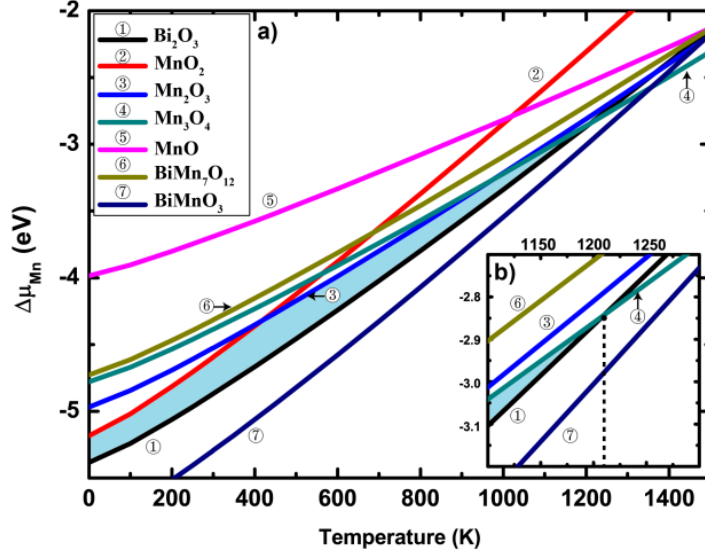
$$4\Delta\mu_{Mn} + 7\Delta\mu_O \geq 2\Delta H_{BiMn_2O_5} - \Delta H_{Bi_2O_3} \quad (19)$$

$$\Delta\mu_{Mn} - 2\Delta\mu_O \geq \Delta H_{BiMn_2O_5} - \Delta H_{BiMnO_3} \quad (20)$$

$$5\Delta\mu_{Mn} + 7\Delta\mu_O \leq \Delta H_{BiMn_7O_{12}} - \Delta H_{BiMn_2O_5} \quad (21)$$

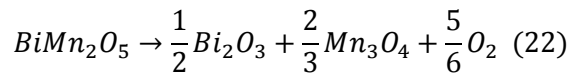
Eq. (15)~(17) are used to confine the region where no metallic or gaseous phase are energetically favorable. Eq. (18)~(19) are defining the binary compounds are unstable and Eq. (20)~(21) guarantees the other ternary phases are not precipitating on the pure  $BiMn_2O_5$  phase. Since entropy of oxygen gas is a function of temperature and pressure according to Eq. (9),  $\Delta\mu_O$  has been converted into temperature contribution under normal calcination condition (1 atm; 20% oxygen partial pressure).

Figure 5(a) shows  $\Delta\mu_{Mn}$  plotted as a function of temperature. Solid lines in the diagram indicates  $\Delta\mu_{Mn}$  that equalize the boundary inequalities (Eq.(15)~(21)) and labeled according to the corresponded compounds. Stable regions fulfilling the boundary conditions are shaded in the figure. The upper limit of the stable region is dominated by the phase evolution of manganese binary oxides: 420K from  $MnO_2$  (Line ②) to  $Mn_2O_3$  (Line ③) and 1020K from  $Mn_2O_3$  to  $Mn_3O_4$  (Line ④). The lower limit of  $BiMn_2O_5$  stable region is governed by  $Bi_2O_3$  (Line ①) instead of the perovskite phase  $BiMnO_3$  (Line ⑦).



**Figure 5** Temperature phase diagram of  $\text{BiMn}_2\text{O}_5$  compounds.  $\Delta\mu_{Mn}$  is plotted as a function of temperature. Compounds considered in the figure are labeled to ① $\text{Bi}_2\text{O}_3$ ② $\text{MnO}_2$ ③ $\text{Mn}_2\text{O}_3$ ④ $\text{Mn}_3\text{O}_4$ ⑤ $\text{MnO}$ ⑥ $\text{BiMn}_7\text{O}_{12}$ ⑦ $\text{BiMnO}_3$ . (a) Overall temperature region and (b) zoomed high temperature fragment corresponding to the decomposition temperature.

Eventually, the crossover of  $\text{Bi}_2\text{O}_3$  and  $\text{Mn}_3\text{O}_4$  defines the limit of  $\text{BiMn}_2\text{O}_5$  stable region, for no longer there is a region that fulfills the boundary conditions to stabilize  $\text{BiMn}_2\text{O}_5$  compounds. Figure 5(b) shows the limit for stable  $\text{BiMn}_2\text{O}_5$  under normal calcination condition is predicted to be 1210K as indicated. Our simulations also have predicted the possible decomposition reaction according to the two crossed over lines of binary compounds since the crossover only stabilize  $\text{Bi}_2\text{O}_3$  and  $\text{Mn}_3\text{O}_4$  (Eq. (18)  $x=3$ ,  $y=4$  case and Eq.(19) are not fulfilled.). The reaction of the decomposition is predicted as:



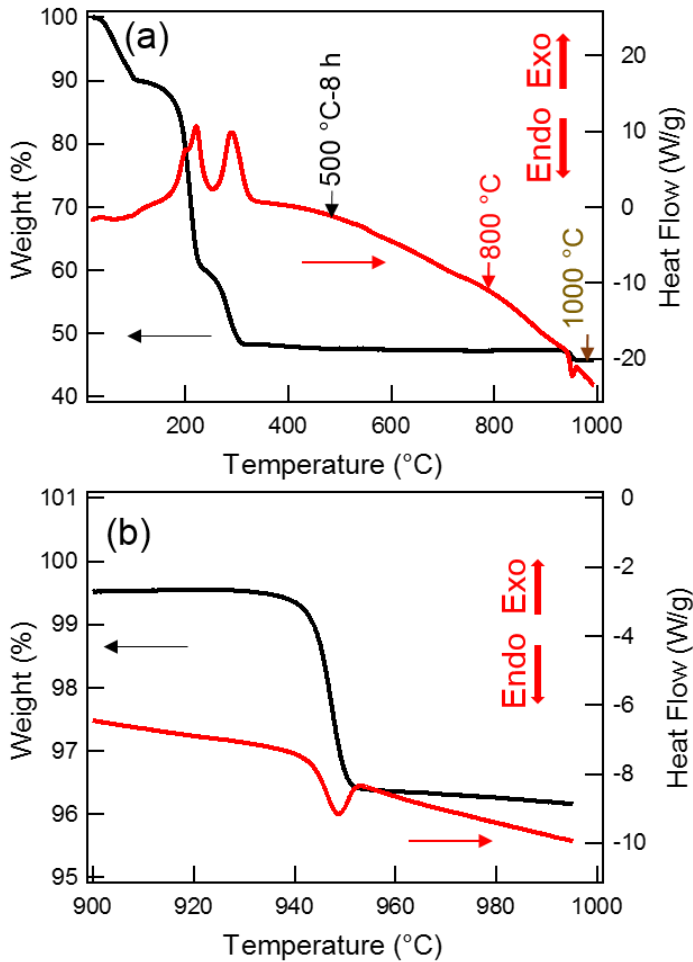


**Figure 6** (a) TGA (Weight %, black) and DSC (Heat flow (W/g), red) curves of BiMn<sub>2</sub>O<sub>5</sub> dried powder. (b) TGA (Weight %, black) and DSC (Heat flow (W/g), red) curves of pure phase BiMn<sub>2</sub>O<sub>5</sub> near decomposition temperature range.

Such prediction has been proven to agree with the experimental data in our unpublished TGA/DSC experimental data shown in Figure 6, where an obvious weight loss is present under the temperature of 1217K.

### 3.2.2 RMn<sub>2</sub>O<sub>5</sub> (R=Pr, Sm, Gd or Y)

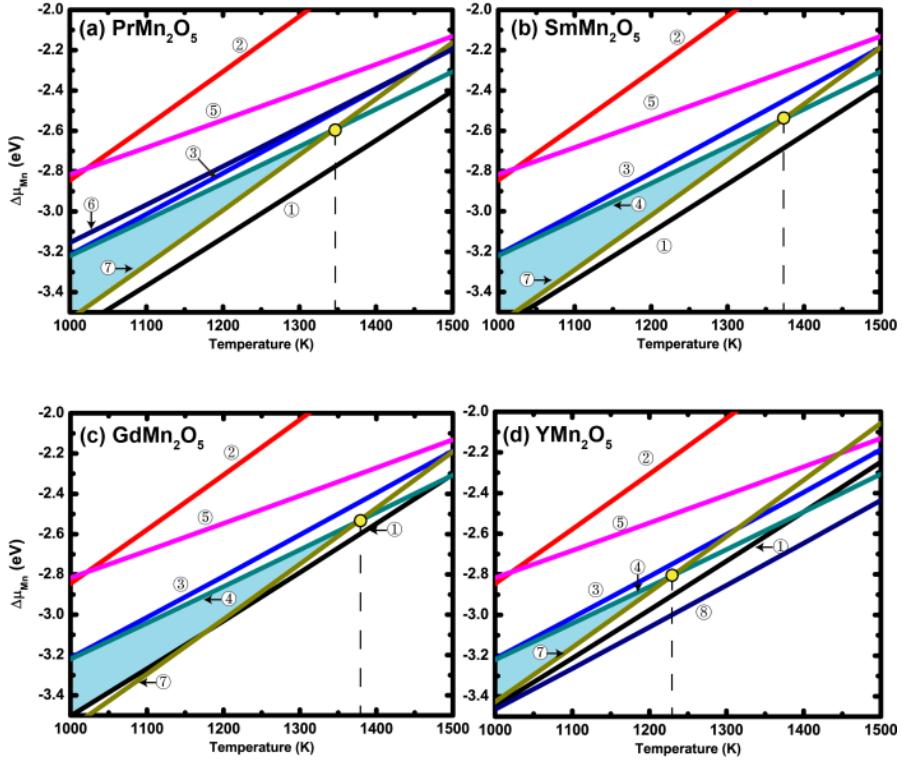


**Figure 7** Temperature phase diagram of (a)  $\text{PrMn}_2\text{O}_5$ , (b)  $\text{SmMn}_2\text{O}_5$ , (c)  $\text{GdMn}_2\text{O}_5$  and (d)  $\text{YMn}_2\text{O}_5$  compounds.  $\Delta\mu_{Mn}$  is plotted as a function of temperature. Compounds considered in the figure are labeled to ①  $\text{R}_2\text{O}_3$  ②  $\text{MnO}_2$  ③  $\text{Mn}_2\text{O}_3$  ④  $\text{Mn}_3\text{O}_4$  ⑤  $\text{MnO}$  ⑥  $\text{PrMn}_7\text{O}_{12}$  ⑦  $\text{RMnO}_3$  ⑧  $\text{Y}_2\text{Mn}_2\text{O}_7$  (R is corresponding to the simulated rare earth elements in the compounds).

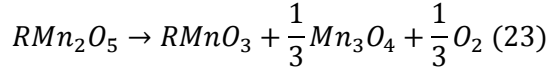
The stability of other  $\text{RMn}_2\text{O}_5$  compounds (R=Pr, Sm, Gd or Y) has also been studied in this thesis. Figure 7 shows the temperature phase diagram of  $\text{RMn}_2\text{O}_5$  (R=Pr, Sm, Gd or Y) compounds. Similar to figure 3, change of manganese chemical potential is plotted as a function of temperature. Apart from the binary compounds (Line ①~⑤) as well as the  $\text{RMnO}_3$  perovskite phases (Line ⑦), ternary compounds:  $\text{PrMn}_7\text{O}_{12}$  (Line ⑥) and  $\text{Y}_2\text{Mn}_2\text{O}_7$  (Line ⑧) has also been

taken into consideration. Eq. (15)~(20) used previously in BiMn<sub>2</sub>O<sub>5</sub> has also been applied to obtain the figure whereas PrMn<sub>7</sub>O<sub>12</sub> and Y<sub>2</sub>Mn<sub>2</sub>O<sub>7</sub> lines are obtained by equalizing Eq. (23)~ (24).

$$5\Delta\mu_{\text{Mn}} + 7\mu_{\text{O}} \leq \Delta H_{\text{PrMn}_7\text{O}_{12}} - \Delta H_{\text{PrMn}_2\text{O}_5} \quad (23)$$

$$2\Delta\mu_{\text{Mn}} + 3\Delta\mu_{\text{O}} \geq 2\Delta H_{\text{YMn}_2\text{O}_5} - \Delta H_{\text{Y}_2\text{Mn}_2\text{O}_7} \quad (24)$$

In figure 7, on one hand, the upper limits of the stable RMn<sub>2</sub>O<sub>5</sub> compounds are confined by the phase evolution of binary oxides since they are independent from the change of R site. On the other hand, the R sites are found to have a major impact on the lower boundary of the RMn<sub>2</sub>O<sub>5</sub> stable regions. Unlike BiMn<sub>2</sub>O<sub>5</sub> compounds, (figure 3), the crossover of Line ⑦ and Line ① (figure 5(a)~(d)) indicates that perovskite RMnO<sub>3</sub> phases are becoming energetically more favorable comparing to the binary R<sub>2</sub>O<sub>3</sub> phases in high temperature region. In YMn<sub>2</sub>O<sub>5</sub> circumstances (figure S4), Y<sub>2</sub>Mn<sub>2</sub>O<sub>7</sub> (Line ⑧) is found to define the boundary of YMn<sub>2</sub>O<sub>5</sub> instead of Y<sub>2</sub>O<sub>3</sub> in less than 1000K. However, near the decomposition temperature, perovskite YMnO<sub>3</sub> (Line ⑦) has been found to cross Y<sub>2</sub>Mn<sub>2</sub>O<sub>7</sub> and defines the final lower boundary region of YMn<sub>2</sub>O<sub>5</sub> stable region. The limit temperature of the stable RMn<sub>2</sub>O<sub>5</sub> region is consequently predicted to be the intersection of Mn<sub>3</sub>O<sub>4</sub> (Line ④) and RMnO<sub>3</sub> (Line ⑦). The yellow spots in the figure indicating the decompose temperature are predicted to be 1340K for PrMn<sub>2</sub>O<sub>5</sub>, 1370K for SmMn<sub>2</sub>O<sub>5</sub>, 1380K for GdMn<sub>2</sub>O<sub>5</sub> and 1220K for YMn<sub>2</sub>O<sub>5</sub>. Furthermore, reactions of the decomposition are predicted to be:



Such prediction is identical to the previous experimental observation where  $\gamma$ - $Mn_3O_4$  and perovskite phase  $RMnO_3$  are observed to be the decomposed compounds.<sup>35</sup>

### 3.3 Error Analysis

As stated in the previous section, there are difference between the DFT predictions and our experiment validation. Figure 8(a) show the decomposition temperature as a function of  $R^{3+}$  ionic Radii in  $RMn_2O_5$  compounds. The simulated temperatures and tendencies are found to be highly correlated to the experiment values where decomposition temperature increases as the ionic radii decrease in Bi and RE elements. Our simulations also give accurate prediction towards the light element yttrium decomposition temperature where the tendency breaks down. Nevertheless, our simulations underestimate almost all the decomposition temperature of the tested compounds where the largest error is observed in  $YMn_2O_5$  compounds with 200K (Shown in figure 8(b)). Other heavy element compounds such as Bi and rare earth elements, on the other hand have shown less than 100K error comparing to the experiments.

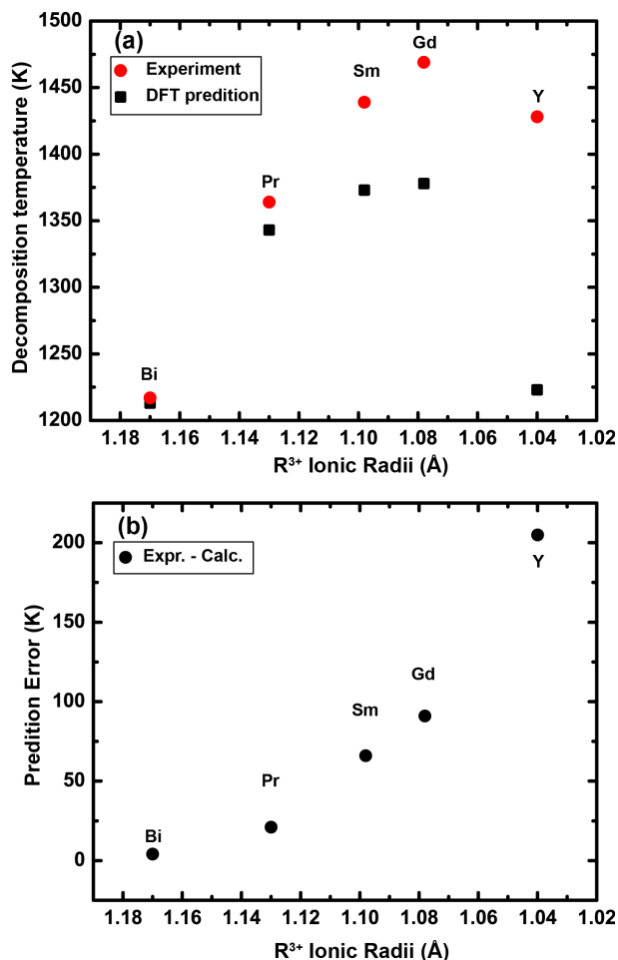


**Figure 8** (a) Diagram of the calculated (red circle), experimental decomposition temperature (black square) of RMn<sub>2</sub>O<sub>5</sub> compounds as a function of R<sup>3+</sup> ionic Radii. (b) Difference between DFT prediction and experiment value of decomposition temperature (prediction error) as a function of R<sup>3+</sup> ionic Radii

Such inconsistency between simulation and experimental observation could not be ignored for practical prediction, even though the errors of DFT prediction are observed to be within 6% for all the tested heavy elements, which is a big step for accurate first principle thermal dynamic calculations (0.1 eV different in formation enthalpy representing about 100K difference in predicted

temperature). In figure 8(b), the monotonic increase of the prediction error along with the ionic radii of the R site elements indicating that further improvement of the predicting accuracy could be achieved.

**Table 4** Temperature difference between experiment and simulation and orbital charge for  $R^{3+}$  ions in  $RMn_2O_5$

$R^{3+}$ in $RMn_2O_5$	Temperature Difference (K)	$d$ orbital charge	$f$ orbital charge
Bi	4	0.243	-
Pr	21	0.676	-
Sm	71	0.788	-
Gd	91	1.106	-
Y	198	0.871	0.122

In Table 4, we look into the orbital charge of R site elements (3<sup>rd</sup>, 4<sup>th</sup> column of the table). Bi shows few  $d$  orbital signals from the projection of the charge density projection since the valance electrons for Bi are mainly  $6s$  and  $6p$  electrons. Rare earth elements shows certain amount of  $d$  orbital charges and no  $f$  orbital signals since in the element pseudopotentials the lanthanide  $4f$  electrons are all treated as the  $d$  electrons and core electrons to give correction description. The  $d$  orbital charge is also increasing with the atomic number of the rare earth elements. Yttrium, on the other hand, shows  $f$  orbital contributions since the energy level of  $4d$  (-1.6291 eV) and  $4f$  (-1.3606 eV) orbitals are very close to each other in the potential, therefore, when forming Y-O bonds, it is highly possible for Y  $4f$  to gain some occupancy. As the 2<sup>nd</sup> column of table 4 shown, error of the DFT prediction increases as the charge of  $d$  orbital in Bi and rare earth elements increases. With both  $d$  and  $f$  orbital charge, Y in  $YMn_2O_5$

has introduce more error than other elements due to the limit of density functional theory. Therefore, we suspect the prediction error could be subject to the inaccurate description of highly correlated  $d/f$  electrons in our simulation.

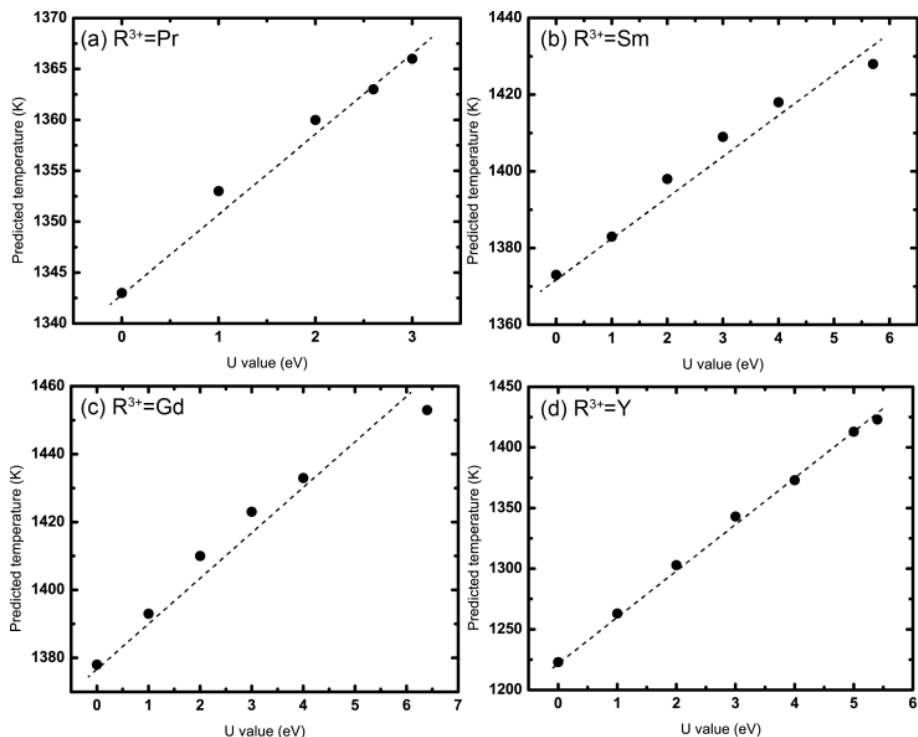


**Figure 9** DFT predicted decomposition temperature as a function of onsite coulomb correction value U: (a)  $\text{PrMn}_2\text{O}_5$ , (b)  $\text{SmMn}_2\text{O}_5$ , (c)  $\text{GdMn}_2\text{O}_5$  and (d)  $\text{YMn}_2\text{O}_5$  compounds.

To confirm our assumption, we again employ the same onsite coulomb correction used for correcting Mn  $d$  electrons on heavy elements. Figure 8 shows our correction effects on  $\text{RMn}_2\text{O}_5$  compounds ( $R=\text{Pr, Sm, Gd}$  or  $\text{Y}$ ). The predicted decomposition temperatures have been found to increase steadily with the increase of correction value U approaching the experimental value.

**Table 5** Simulated and experiment decomposition temperature after R site ion U correction

R <sup>3+</sup> in RMn <sub>2</sub> O <sub>5</sub>	R <sup>3+</sup> U value (eV)	Temperature before U correction (K)	Temperature after U correction (K)	Experiment temperature (K)
Bi	0	1213	-	1217
Pr	2.6	1343	1363	1364
Sm	5.7	1373	1428	1439
Gd	6.4	1378	1453	1469
Y	5.4	1223	1423	1458

In Table 5, we summarized our fitted U correction parameters used for giving the accurate prediction temperature and also the corrected temperatures are compared with the uncorrected as well as the experiment observation. The obtained decomposition temperature after corrections for RMn<sub>2</sub>O<sub>5</sub> compounds shows consistency with our experiment decomposition temperatures, therefore, could give a good prediction on the compounds stability.

## Chapter 4 Conclusion

The thermal stability of  $\text{RMn}_2\text{O}_5$  compounds was studied by employing a high efficiency thought-output first principle simulation approach. Reactions of decomposition and decomposition temperature have been predicted and compared with experiments. We found that DFT predicted temperature phase diagram could give good description of the decomposition reactions comparing with our experimental observations. However, without any further GGA+U corrections on the  $\text{R}^{3+}$  ions in  $\text{RMn}_2\text{O}_5$  compounds, the predicted decomposition temperatures are found to underestimate the decomposition temperatures of the rare earth and Y involved  $\text{RMn}_2\text{O}_5$  oxide compounds. Furthermore, the underestimations of the decomposition temperature are found correlated to the localized  $d/f$  orbital charge, which is inaccurately described in DFT simulations. Hence, GGA+U corrections on R site elements are further investigated and found to give improved description on the decomposition temperature of  $\text{RMn}_2\text{O}_5$  compounds.

## Bibliography

1. Jin, S.; Hubert, A. G.; Naoaki, Y.; Haruyuki, N.; John, B. G.; Yang, S.-H., Design principles for oxygen-reduction activity on perovskite oxide catalysts for fuel cells and metal–air batteries. *Nature Chemistry* **2011**, 3, (7), 546-550.
2. Korotcenkov, G.; Cho, B. K., Instability of metal oxide-based conductometric gas sensors and approaches to stability improvement (short survey). *Sensors and Actuators B: Chemical* **2011**.
3. Weichao, W.; Geoffrey, M.; Neeti, K.; Guang, Y.; Bin, S.; Matt, N.; Uschi, M. G.; Burtron, H. D.; Gary, J.; Kyeongjae, C.; Xianghong, H., Mixed-phase oxide catalyst based on Mn-mullite (Sm, Gd)Mn<sub>2</sub>O<sub>5</sub> for NO oxidation in diesel exhaust. *Science (New York, N.Y.)* **2012**, 337, (6096), 832-835.
4. Anubhav, J.; Geoffroy, H.; Shyue Ping, O.; Charles, J. M.; Christopher, C. F.; Kristin, A. P.; Gerbrand, C., Formation enthalpies by mixing GGA and GGA + U calculations. *Physical Review B* **2011**, 84.
5. Lei, W.; Thomas, M.; Gerbrand, C., Oxidation energies of transition metal oxides within the GGA+U framework. *Physical Review B* **2006**, 73.
6. Wang, L.; Maxisch, T.; Ceder, G., A First-Principles Approach to Studying the Thermal Stability of Oxide Cathode Materials. *Chemistry of Materials* **2007**, 19.
7. Denis, K.; Gerbrand, C., Tailoring the Morphology of LiCoO<sub>2</sub>: A First Principles Study. *Chemistry of Materials* **2009**, 21.

8. Shyue Ping, O.; Lei, W.; Byoungwoo, K.; Gerbrand, C., Li-Fe-P-O<sub>2</sub>Phase Diagram from First Principles Calculations. *Chemistry of Materials* **2008**, 20.
9. Georg Kresse, M. M., and Jürgen Furthmüller VASP online Guide. [http://cms.mpi.univie.ac.at/vasp/vasp/elements\\_1.html](http://cms.mpi.univie.ac.at/vasp/vasp/elements_1.html) (12/18),
10. Chevrier, V. L.; Ong, S. P.; Armiento, R.; Chan, M. K. Y.; Ceder, G., Hybrid density functional calculations of redox potentials and formation energies of transition metal compounds. *Physical Review B* **2010**.
11. YongMan, C.; David, S. M.; Lin, M. C.; Meilin, L., Oxygen Reduction on LaMnO<sub>3</sub>-Based Cathode Materials in Solid Oxide Fuel Cells. *Chemistry of Materials* **2007**.
12. Hur, N.; Park, S.; Sharma, P. A.; Ahn, J. S.; Guha, S.; Cheong, S. W., Electric polarization reversal and memory in a multiferroic material induced by magnetic fields. *Nature* **2004**, 429, (6990), 392-395.
13. Songmei, S.; Wenzhong, W.; Ling, Z.; Meng, S., Visible Light-Induced Photocatalytic Oxidation of Phenol and Aqueous Ammonia in Flowerlike Bi<sub>2</sub>Fe<sub>4</sub>O<sub>9</sub>Suspensions. *The Journal of Physical Chemistry C* **2009**, 113.
14. Bloom, I.; Hash, M. C.; Zebrowski, J. P.; Myles..., K. M., Oxide-ion conductivity of bismuth aluminates. *Oxide-ion conductivity of bismuth aluminates* **1992**.
15. Hartmut, S.; Sridhar, K., Mullite. *Mullite* **2006**.
16. Kresse, G.; Furthmuller, J., Efficiency of ab-initio total energy calculations for metals and semiconductors using a plane-wave basis set. *Computational Materials Science* **1996**, 6, (1), 15-50.

17. Kresse, G.; Furthmuller, J., Efficient iterative schemes for ab initio total-energy calculations using a plane-wave basis set. *Physical Review B* **1996**, 54, (16), 11169-11186.
18. Langreth, D. C.; Mehl, M. J., Beyond the Local-Density Approximation in Calculations of Ground-State Electronic-Properties. *Physical Review B* **1983**, 28, (4), 1809-1834.
19. Dudarev, S. L.; Botton, G. A.; Savrasov, S. Y.; Humphreys, C. J.; Sutton, A. P., Electron-energy-loss spectra and the structural stability of nickel oxide: An LSDA+U study. *Physical Review B* **1998**, 57, (3), 1505-1509.
20. Hendrik, J. M.; James, D. P., Special points for Brillouin-zone integrations. *Physical Review B* **1976**.
21. Doubrovsky, C.; Andr e G.; Gukasov, A.; Auban-Senzier, P.; Pasquier, C. R.; Elkaim, E.; Li, M.; Greenblatt, M.; Damay, F.; Foury-Leylekian, P., Magnetic phase transitions in  $\text{PrMn}_{2}\text{O}_{5}$ : Importance of ion-size threshold size effects in  $\text{RMn}_{2}\text{O}_{5}$  compounds (R = rare earth). *Physical Review B* **2012**.
22. Lee, N.; Vecchini, C.; Choi, Y. J.; Chapon, L. C.; Bombardi, A.; Radaelli, P. G.; Cheong, S. W., Giant Tunability of Ferroelectric Polarization in  $\text{GdMn}_{2}\text{O}_{5}$ . *Physical Review Letters* **2013**.
23. Vecchini, C.; Chapon, L.; Brown, P.; Chatterji, T.; Park, S.; Cheong, S. W.; Radaelli, P., Commensurate magnetic structures of  $\text{RMn}_{2}\text{O}_{5}$  (R=Y, Ho, Bi) determined by single-crystal neutron diffraction. *Physical Review B* **2008**.
24. Roth, W. L., Magnetic Structures of MnO, FeO, CoO, and NiO. *Physical Review* **1958**, 110, (6), 1333-1341.

25. Regulski, M.; Przeniosło, R.; Sosnowska, I.; Hoffmann, J. U., Incommensurate magnetic structure of  $\beta$ -MnO<sub>2</sub>. *Physical Review B* **2003**, 68.
26. Regulski, M.; Przeniosło, R.; Sosnowska, I.; Hohlwein, D.; Schneider, R., Neutron diffraction study of the magnetic structure of  $\alpha$ -Mn<sub>2</sub>O<sub>3</sub>. *Journal of Alloys and Compounds* **2004**, 362, (1-2), 236-240.
27. Alain, C.; Philippe, D. A.; Roberto, D.; Victor, S., Ab initio Hartree-Fock investigation of the structural, electronic, and magnetic properties of Mn<sub>3</sub>O<sub>4</sub>. *Physical Review B* **1999**, 60.
28. Oswald, K.; Charles, B. A.; Spencer, P. J., Materials thermochemistry. *Materials thermochemistry* **1993**.
29. Yu, A. M.; Heifets, E.; Kotomin, E. A.; Maier, J., Atomic, electronic and thermodynamic properties of cubic and orthorhombic LaMnO<sub>3</sub> surfaces. *Surface Science* **2009**.
30. Chase, M. W.; Curnutt, J. L.; Downey, J. R.; McDonald, R. A.; Syverud, A. N.; Valenzuela, E. A., JANAF Thermochemical Tables, 1982 Supplement. *Journal of Physical and Chemical Reference Data* **1982**, 11, (3), 695.
31. Granado, E.; Eleot ério, M.; Garc ía-Flores, A.; Souza, J.; Golovenchits, E.; Sanina, V., Magnetoelastic and thermal effects in the BiMn<sub>2</sub>O<sub>5</sub> lattice: A high-resolution x-ray diffraction study. *Physical Review B* **2008**.
32. Kenzo, K.; Hiroyuki, O.; Yusuke, I.; Keisuke, S.; Saori, M., Phase Equilibrium in the System Ln–M–O. *Journal of Solid State Chemistry* **2002**.
33. Kenzo, K.; Minehito, K.; Takashi, K., Phase Equilibrium in the System Ln–Mn–O IV. Ln=Sm at 1100 °C. *Journal of Solid State Chemistry* **2002**.

34. Franchini, C.; Podloucky, R.; Paier, J.; Marsman, M.; Kresse, G., Ground-state properties of multivalent manganese oxides: Density functional and hybrid density functional calculations. *Physical Review B* **2007**, 75.
35. Vedmid, L. B.; Fedorova, O. M.; Yankin, A. M.; Balakirev, V. F.; Yu, V. G., Phase diagrams and ranges of cation homogeneity for systems composed of oxides of manganese and 4f rare earth elements (La57-Lu71), oxides of manganese and Sc21, and oxides of manganese and Y39. *Bulletin of the Russian Academy of Sciences: Physics* **2013**.

## 초 록

밀도함수이론에 근거한 매우 효율적인 계산적 검사 방법은 많은 발전을 이루어 왔다. 그러나 천이 금속 산화 합성물로 사용되는 재료들의 열적 안정성을 계산하는 것은 아직 과제로 남아있다. 이 연구에서는 혼합 GGA와 GGA+U 의 방법을 이용하여, 위의 재료들의 열적 안정성을 검사하였다. 온도 상변화 그림은 DFT 시뮬레이션으로부터 구성하였으며 합성물들을 잘 예측할 수 있다. 그러나 예측된 온도는 실험데이터에 비해 작은 수치로 계산된다. 이것은 R 요소의 d/f 오비탈 충전이 부정확한 시뮬레이션의 원인이 되었다는 것을 알 수 있었다. 이 연구의 GGA+U의 보정은 좀더 정확한 결과를 보여주어 다른 계산적 방법 없이도 열적 안정성 예측의 정확도를 개선할 수 있었다.